Unfiltering Earth Radiation Budget Experiment (ERBE) Scanner Radiances Using the CERES Algorithm and Its Evaluation with Nonscanner Observations

ALOK K. SHRESTHA

Science Systems and Applications Inc., and NASA Langley Research Center, Hampton, Virginia

SEIJI KATO AND TAKMENG WONG

NASA Langley Research Center, Hampton, Virginia

DAVID A. RUTAN, WALTER F. MILLER, FRED G. ROSE, G. LOUIS SMITH, AND KRISTOPHER M. BEDKA

Science Systems and Applications Inc., and NASA Langley Research Center, Hampton, Virginia

PATRICK MINNIS

NASA Langley Research Center, Hampton, Virginia

JOSE R. FERNANDEZ

Science Systems and Applications Inc., and NASA Langley Research Center, Hampton, Virginia

(Manuscript received 11 April 2013, in final form 22 November 2013)

ABSTRACT

The *NOAA-9* Earth Radiation Budget Experiment (ERBE) scanner measured broadband shortwave, longwave, and total radiances from February 1985 through January 1987. These scanner radiances are reprocessed using the more recent Clouds and the Earth's Radiant Energy System (CERES) unfiltering algorithm. The scene information, including cloud properties, required for reprocessing is derived using Advanced Very High Resolution Radiometer (AVHRR) data on board *NOAA-9*, while no imager data were used in the original ERBE unfiltering. The reprocessing increases the *NOAA-9* ERBE scanner unfiltered longwave radiances by 1.4%–2.0% during daytime and 0.2%–0.3% during nighttime relative to those derived from the ERBE unfiltering algorithm. Similarly, the scanner unfiltered shortwave radiances increase by ~1% for clear ocean and land and decrease for all-sky ocean, land, and snow/ice by ~1%. The resulting *NOAA-9* ERBE scanner unfiltered radiances are then compared with *NOAA-9* nonscanner irradiances by integrating the ERBE scanner radiance over the nonscanner field of view. The comparison indicates that the integrated scanner radiances are larger by 0.9% for shortwave and 0.7% smaller for longwave. A sensitivity study shows that the one-standard-deviation uncertainties in the agreement are ±2.5%, ±1.2%, and ±1.8% for the shortwave, nighttime longwave, and daytime longwave irradiances, respectively. The *NOAA-9* and ERBS nonscanner irradiances are also compared using 2 years of data. The comparison indicates that the *NOAA-9* nonscanner shortwave, nighttime longwave, and daytime longwave irradiances are 0.3% larger, 0.6% smaller, and 0.4% larger, respectively. The longer observational record provided by the ERBS nonscanner plays a critical role in tying the CERES-like *NOAA-9* ERBE scanner dataset from the mid-1980s to the present-day CERES scanner data record.

1. Introduction

To better understand the earth radiation budget and its effect on climate, it is essential to monitor, as accurately as possible, the exchange of shortwave and

Corresponding author address: Alok K. Shrestha, Science System and Applications Inc., 1 Enterprise Parkway, Suite 200, Hampton, VA 23666.
E-mail: alok.k.shrestha@nasa.gov

DOI: 10.1175/JTECH-D-13-00072.1

© 2014 American Meteorological Society

longwave radiation at the top of the atmosphere (TOA) over many years. Recognizing this need, the Earth Radiation Budget Experiment (ERBE) was initiated in the late 1970s and conducted during the second half of the 1980s (Barkstrom 1984; Barkstrom and Smith 1986). ERBE instruments were on board three Earth-orbiting satellites: the National Aeronautics and Space Administration (NASA) Earth Radiation Budget Satellite (ERBS) and two National Oceanic and Atmospheric Administration (NOAA) satellites (*NOAA-9* and *NOAA-10*). Each satellite in the ERBE mission carried a scanning radiometer and a nonscanner package (Barkstrom 1984). The ERBE scanners had three detectors: total, shortwave, and longwave channels. The nonscanner instruments had Earth-viewing detectors and a total solar irradiance monitor (Luther et al. 1986). The wide field-of-view (WFOV) nonscanner had a limb-to-limb Earth view, while it was limited to about 1000 km in diameter (Barkstrom 1984) for the medium field-of-view (MFOV) instrument. Each set of MFOV and WFOV detectors consisted of a shortwave channel and a total channel. Together, the three scanners measured the regional radiation budget between 1985 and 1989, while the WFOV and MFOV nonscanners operated much longer. The ERBS nonscanners produced the longest record, measuring the large-scale nonpolar radiation budget from 1985 to 1999.

A more sophisticated scanner and methodologies for interpreting the measurements were developed for the Clouds and the Earth's Radiant Energy System (CERES), the NASA successor to ERBE (Wielicki et al. 1998). The first CERES scanners were launched in 1998 on the Tropical Rainfall Monitoring Mission, but acquired data for only 9 months. However, CERES instruments have been operating successfully on the *Terra* and *Aqua* satellites since 2000 and 2002, respectively. To study long-term changes in the earth radiation budget, it is necessary to normalize, as accurately as possible, the ERBE and CERES data to cover the period from 1985 to the present. To effect that normalization, it is necessary to account for instrument and measurement interpretation differences. One approach is first to process the ERBE scanner data using CERES methodologies and then to normalize nonscanner measurements to collocated scanner data. This method should yield a dataset that is consistent as possible with CERES, save for calibration differences. This paper takes the first step in normalizing the CERES and ERBE scanner data.

To estimate TOA irradiance from ERBE scanner radiance observations, two steps are involved: spectral correction (unfiltering) and conversion of radiance to irradiance (inversion). Radiances entering the instrument are modified by the spectral response of each channel. The method used to retrieve radiance from the measured value, by removing the effects of nonuniform spectral response along the optical path of the instrument, is called unfiltering (Green and Avis 1996). This unfiltered radiance is then converted to TOA irradiance, the inversion process, using scene-dependent anisotropic directional models that account for the angular dependence of the radiances leaving a given scene (Suttles et al. 1992). Both unfiltering and inversion depend on the scene type (surface and cloud). Thus, the accuracy of these two steps depends upon proper identification of the scene viewed in the ERBE scanner footprints. This paper addresses the unfiltering process.

Our knowledge of unfiltering techniques and treating scene-type anisotropic dependency has advanced since the ERBE data were originally processed. In addition, recent advances in data processing technology allow us to adopt more accurate algorithms that were neither available nor possible to utilize at that time. Application of the algorithms used by CERES has the potential to significantly improve the ERBE-derived TOA irradiances. For example, Loeb et al. (2001) showed that applying the CERES unfiltering scheme to observed ERBS scanner all-sky shortwave radiances increased the unfiltered radiance by 1.7%. Similarly, the all-sky relative differences between CERES and ERBE were reduced to 0.6% (1.9%) from 1.1% (2.1%) for day (night) longwave. A study by Wong et al. (2006) suggested that the tropical TOA shortwave and longwave irradiance changes over a decade are $-2.1\,\mathrm{W\,m^{-2}}$ (-2.2%) and $0.7\,\mathrm{W\,m^{-2}}$ (0.3%), respectively. It is clear that differences in the unfiltering process must be removed as much as possible to determining decadal variations in the radiation budget from CERES and ERBE scanner observations. For this reason we plan to process ERBE data with algorithms similar to those used by CERES and minimize algorithm differences.

The flow diagram of the proposed process is shown in Fig. 1. While Fig. 1 outlines the entire proposed processing scheme, this paper focuses on the unfiltering process of ERBE scanner radiances using the CERES unfiltering algorithm as described in Loeb et al. (2001).

The details of the ERBE instruments are discussed in section 2. Section 3 briefly discusses the CERES unfiltering algorithm and its difference with the ERBE algorithm. Section 4 compares unfiltered radiances derived using these two algorithms. Section 5 addresses the calibration of the *NOAA-9* ERBE scanner by comparing its measurements with irradiances observed by *NOAA-9* nonscanner, following the approach described in Green et al. 1990. Because ERBS nonscanner observations overlap with CERES TRMM observations, and its calibration was evaluated in earlier studies (Rutan

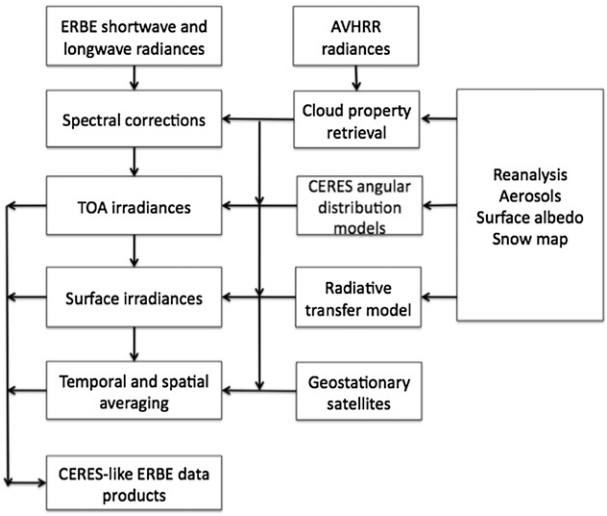

FIG. 1. Flow diagram of ERBE data processing with CERES algorithms.

et al. 2001), *NOAA-9* nonscanner observations are also evaluated by comparing them with ERBS nonscanner observations in section 6.

2. ERBE scanner, nonscanner, and Advanced Very High Resolution Radiometer imager instruments

The ERBS was launched 5 October 1984 in a precessing orbit at an altitude of 610 km with an inclination of 57° (Green and Avis 1996). *NOAA-9* was launched 12 December 1984 into a polar sun-synchronous orbit at an altitude of 812 km, an inclination of 99°, and an equatorial crossing time of 1430 UTC (Kopia 1986). The *NOAA-10* was launched 17 September 1986 in a 98°-inclined sun-synchronous orbit at an altitude of 833 km with an equatorial crossing time of 0730 UT. Both NOAA satellites were in ascending node (Luther et al. 1986). The operational period of various instruments on these three satellites is shown in Table 1 (Barkstrom and Kibler 2013; Vincent 2013). As previously mentioned each satellite in the ERBE mission carried a narrow field-of-view (FOV) ERBE scanner and nonscanner (Barkstrom 1984) instruments. The ERBE scanners had three detectors: a total (TOT) channel that had no filter and absorbed radiation in a wavelength range from approximately 0 to 200 μm; a shortwave (SW) channel that had a fused silica filter that transmitted wavelengths from approximately 0.2 to 5 μm; and a longwave (LW) channel that had a multilayer filter on a diamond substrate, which transmitted radiation at wavelengths from 5 to 50 μm (Kopia 1986). Each detector scanned the Earth perpendicular to the satellite ground track from horizon to horizon. All detectors were thermistor bolometers and received radiation gathered by an f/1.84 Cassegrain telescope, whose aluminum-coated mirrors were overcoated to enhance ultraviolet reflectivity. To enhance the spectral flatness of the detectors, each thermistor chip was coated with a thin layer of black paint. All three ERBE scanner channels had a field stop located at the focal plane of the telescope that gave an instantaneous hexagonal FOV angular size of 3° × 4.5°, the longer dimension being along the satellite ground track (Barkstrom 1984). Because of the altitude differences among the ERBS, *NOAA-9*, and *NOAA-10* orbits mentioned earlier, the respective ERBE scanner nadir footprint sizes at the surface were approximately 32 km × 48 km, 43 km × 64 km, and 43 km × 66 km, respectively (Barkstrom 1984).

In addition to the earth-viewing WFOV and MFOV instruments, the nonscanner on each satellite included a total solar irradiance monitor (Luther et al. 1986). The desired earth-emitted longwave measurement is achieved by subtraction of the signal detected by the nonscanner shortwave channel from total channel radiance (Luther et al. 1986). Similar to the ERBE scanners, the total channel was sensitive to all wavelengths and the shortwave channel used a high purity, fused silica filter dome to transmit only radiation from 0.2 to 5 μm. Because of the concern for spectral flatness and high accuracy, all four channels on the nonscanners were active cavity radiometers (Barkstrom 1984). We only use WFOV nonscanners in this study and hereafter refer to the WFOV instruments as nonscanners.

Also on board the *NOAA-9* and *NOAA-10* is an Advanced Very High Resolution Radiometer (AVHRR), a cross-track scanning imager. The AVHRR recorded narrowband measurements in five spectral channels with a spatial resolution of about ~1 km at nadir, which were subsampled and averaged to produce a ~4-km

TABLE 1. Operational dates of ERBE instruments.

	ERBE scanner		Nonscanner		AVHRR	
Satellite	From	To	From	To	From	To
ERBS	Oct 1984	Feb 1990	Oct 1984	Oct 1999	No AVHRR instrument	
NOAA-9	Jan 1985	Jan 1987	Jan 1985	Nov 1990	Feb 1985	Nov 1988
NOAA-10	Oct 1986	May 1989	Oct 1986	Oct 1994	Nov 1986	Sep 1991

TABLE 2. Spectral characteristics of AVHRR instruments on board ERBE.

Satellite	Channel 1 (μm)	Channel 2 (μm)	Channel 3 (μm)	Channel 4 (μm)	Channel 5 (μm)
NOAA-9	0.58–0.68	0.725–1.10	3.55–3.93	10.3–11.3	11.5–12.5
NOAA-10	0.58–0.68	0.725–1.10	3.55–3.93	10.3–11.3	Channel 4 repeated

global areal coverage dataset. The AVHRR dataset is used in this study (Gruber et al. 1994) to characterize the scene in each ERBE scanner FOV. The spectral characteristics of all five AVHRR channels for *NOAA-9* and *NOAA-10* are listed in Table 2 (USGS 2013).

3. Method

All original ERBE products register footprint locations and their viewing geometry at a 30-km altitude using geocentric coordinates, while CERES products are registered at the surface using geodetic coordinates. To be consistent with the CERES products, ERBE footprint locations and their viewing geometry are registered at the surface using geodetic coordinates. We use the ERBE S8-Processed Archival Tape (PAT) daily product to generate an ERBE instrument Earth scan (IES) product (Kusterer 2013) that contains footprint geolocation. Radiances observed by the ERBE scanner are stored chronologically by footprints in the S8-PAT and are divided into 16-s records (Wong 2013). As mentioned earlier, the effect of instrument spectral response needs to be removed and the reflected (shortwave) and emitted (longwave) radiance need to be separated before the radiance is converted to irradiance. This spectral correction procedure, which handles both processes, is historically called the unfiltering and is discussed in detail in the following section.

a. Unfiltering ERBE scanner filtered radiance

Both the CERES (Loeb et al. 2001) and ERBE (Green and Avis 1996) unfiltering algorithms remove the effect of instrument spectral response from observed radiances but use different techniques. Both techniques require knowledge of each channel's spectral response as well as the spectral nature of observed scene. The ERBE unfiltering technique derives scene information from broadband radiances using a maximum likelihood estimation (MLE) method described in Wielicki and Green (1989). The CERES unfiltering technique derives scene information from imager narrowband radiances collocated inside the larger CERES FOV, providing a more robust scene identification. In this study, *NOAA-9* AVHRR observations are used to derive the scene information. The scene information such as cloud fraction is derived from the *NOAA-9* AVHRR using the techniques of Trepte et al. (2003) and Minnis et al. (2008), while other cloud parameters such as cloud optical depth and phase were retrieved using the methods of Minnis et al. (2011).

As described by Green and Avis 1996 and Loeb et al. 2001, the filtered radiance m_f is expressed as

$$m_f^j = \int_0^\infty S_\lambda^j I_\lambda \, d\lambda \,, \tag{1}$$

where λ is the wavelength, S_λ^j is the normalized spectral response function of the instrument ($0 \le S_\lambda^j \ge 1.0$), I_λ is the spectral radiance incident on the instrument, and the superscript j represents the shortwave, longwave, and total channels.

Both the CERES and ERBE unfiltering algorithms derive the unfiltered radiance m_u from filtered radiance m_f using coefficients derived from modeled spectral radiances (database) of various scenes. However, the spectral database used by Green and Avis (1996) for ERBE (see Arduini 1985) is very different from that used by Loeb et al. (2001) in CERES. The CERES unfiltering uses an updated and substantially larger theoretical spectral radiance database, including a large range of cloud optical thickness and cloud-top heights, thus providing significantly improved coefficients. In addition to different methods to derive scene information, including improved coefficients, the CERES algorithm uses a quadratic term in deriving the shortwave unfiltering radiance (Loeb et al. 2001), while ERBE algorithm assumes a linear relationship.

Following Loeb et al. (2001), the unfiltered radiances for shortwave SW and longwave LW at day D and night N are expressed in Eqs. (2)–(4), given as

$$m_u^{\mathrm{SW}}(D) = a_0 + a_1 m_f^{\mathrm{SW}} + a_2 (m_f^{\mathrm{SW}})^2 \,, \tag{2}$$

$$m_u^{\mathrm{LW}}(D) = b_0 + b_1 m_f^{\mathrm{SW}} + b_2 m_f^{\mathrm{TOT}} + b_3 m_f^{\mathrm{LW}}, \quad \text{and} \tag{3}$$

$$m_u^{\mathrm{LW}}(N) = c_0 + c_1 m_f^{\mathrm{TOT}} + c_2 m_f^{\mathrm{LW}} \,, \tag{4}$$

respectively. The coefficients a_0, a_1, a_2, b_0, b_1, b_2, b_3, c_0, c_1, and c_2 are all theoretically derived by regressing modeled unfiltered and filtered radiances. The shortwave coefficients (a_0, a_1, a_2) are derived as a function of viewing zenith angle, relative azimuth angle, and solar zenith angle, respectively, while the longwave coefficients only depend on viewing zenith angle. In addition, scenes

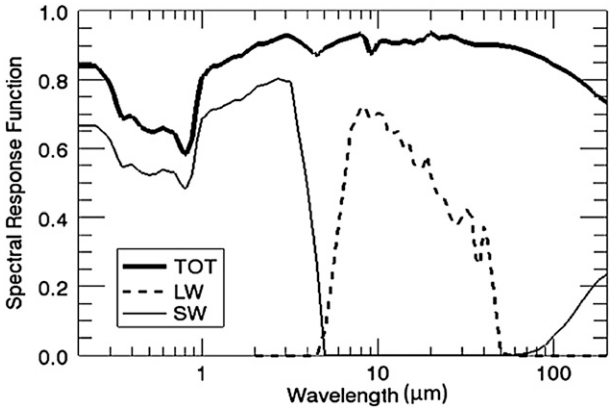

FIG. 2. *NOAA-9* scanning radiometer spectral response functions.

for both shortwave and longwave are separated by clear and overcast conditions, and surface type is separated by snow, land, ocean, and desert. The coefficients for partly (cloud fraction = 0.275) and mostly (cloud fraction = 0.725) cloudy conditions are derived by interpolating between the clear and overcast coefficients. Both the CERES and ERBE algorithms discretize the viewing, relative azimuth, and solar zenith angles to apply the unfiltering coefficient. However, the CERES algorithm uses a linear interpolation of coefficients to minimize a discretization error, while no angular interpolation is used in the ERBE algorithm (Loeb et al. 2001).

Figure 2 shows the *NOAA-9* ERBE scanner spectral response functions. The response function for the longwave portion of the total channel is relatively flat compared to that of the longwave channel. For this reason unfiltered longwave radiance is derived using measurements from the total and shortwave channels. However, the nominal shortwave bandpass allows radiation at wavelengths greater than 50 μm in addition to the nominal spectral interval between 0.2 and 5 μm, thus affecting its reflected measurements. Since this additional radiation is entirely terrestrial in origin, it must be removed from the filtered shortwave radiance to obtain a radiance that is purely solar in origin. The next section discusses our approach to remove the effect of emitted radiance from the shortwave filtered radiance.

b. *Subtraction of emitted radiance from shortwave filtered radiance*

The CERES algorithm subtracts the longwave contribution to the shortwave channel, caused by a small sensitivity at wavelengths larger than 50 μm. To estimate this contribution, the CERES algorithm uses a second-order fit between the CERES window filtered radiances WN and nighttime shortwave filtered radiances as shown in Eq. (5), defined as

$$m_e^{\mathrm{SW}} = k_0 + k_1 m_f^{\mathrm{WN}} + k_2 (m_f^{\mathrm{WN}})^2, \tag{5}$$

where m_e^{SW} is the emitted radiance detected by the shortwave channel. The resulting coefficients are then applied to the daytime window radiances to estimate the longwave contribution to the coincident SW filtered radiances, which is then subtracted during the unfiltering process (Loeb et al. 2001). ERBE scanners however lack the window channel and their longwave channel is noisier than the total channel (Green and Avis 1996). Hence, we reformulate Eq. (5) using computed longwave nadir-view radiances calculated from the Principal Component-based Radiative Transfer Model (PCRTM; Liu et al. 2006). This radiance is then used to estimate the longwave contribution to the shortwave channel theoretically. The temperature and humidity profiles required for this estimation are obtained from the Goddard Earth Observing System Data Assimilation System, levels 4 (GEOS-4) and 5 (GEOS-5), reanalyses (Bloom et al. 2005). Cloud properties are extracted from the *Cloud–Aerosol Lidar and Infrared Pathfinder Satellite Observations* (*CALIPSO*)–*CloudSat*–CERES–Moderate Resolution Imaging Spectroradiometer (MODIS) dataset (Kato et al. 2010). We use four seasonal days of cloud properties to cover a realistic range of cloud types for the computations. The ERBE (*NOAA-9* in this study) spectral response functions for the shortwave and longwave channels are applied to the modeled spectral radiances to simulate filtered longwave radiances and the thermal component of the filtered shortwave radiances. Following Loeb et al. (2001), we use a second-order polynomial, defined as

$$m_e^{\mathrm{SW}} = k_0 + k_1 m_f^{\mathrm{LW}} + k_2 (m_f^{\mathrm{LW}})^2, \tag{6}$$

to fit the shortwave radiances as a function of longwave radiance for four seasonal months independently. We further fit these resulting four seasonal month curves by a second-order polynomial to obtain the final coefficients. Figure 3 shows these second-order polynomial fits between nighttime filtered shortwave and filtered longwave radiances. The final coefficients k_0, k_1, and k_2 are 0.188 894 10, −0.009 721 260, and 0.000 214 334, respectively. These coefficients are then used to estimate the thermal component m_e^{SW} present in the ERBE daytime shortwave filtered radiance. This thermal component is then subtracted from the shortwave filtered radiance to estimate proper shortwave filtered radiance $m_f^{\mathrm{SW}_r}$ as

$$m_f^{\mathrm{SW}_r} = m_f^{\mathrm{SW}} - m_e^{\mathrm{SW}}, \tag{7}$$

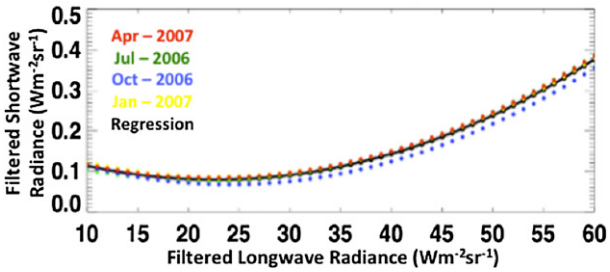

FIG. 3. Relationship between filtered SW and LW radiances for the *NOAA-9* ERBE scanner instrument. The monthly relationship is derived by fitting a second-order polynomial to nadir-view modeled filtered radiances.

where m_f^{SW} is the daytime filtered shortwave (SWDT) radiance. We compute the thermal component for all footprints individually based on the instantaneous ERBE longwave filtered radiance. When the filtered longwave radiance is not available, a default value of $0.173\,75\,\mathrm{W\,m^{-2}\,sr^{-1}}$ (mean value of the nighttime filtered shortwave radiance) is used for subtraction. Note that the thermal component is approximately 0.26% relative to the global mean unfiltered radiance detected by the shortwave channel.

4. Comparison of ERBE-SSF and S8-PAT unfiltered radiances

In this section we compare unfiltered radiances from the CERES and ERBE algorithms to quantify the differences between the algorithms. For the comparison we compute the average unfiltered radiances over 4 months for clear ocean, clear land, all-sky ocean, all-sky land, and all-sky snow/ice backgrounds. To obtain all-sky snow/ice, we use all footprints in the latitude ranges of 60°–90°N and 60°–90°S. Results of these comparisons are summarized in Tables 3–5.

Tables 3 and 4 show that daytime and nighttime longwave unfiltered radiances, respectively, derived using the CERES unfiltering algorithm [labeled ERBE Single Scanner Footprint (SSF)] are, on average, larger than those derived from the ERBE algorithm (labeled ERBE S8) for all scene types mentioned earlier. The CERES algorithm increases the unfiltered daytime longwave (LWDT) radiance by 1.5% and 1.7% for clear and all-sky ocean, respectively; 1.4% and 2.0% for clear and all-sky land, respectively; and 1.5% for all-sky snow/ice. Similarly, the unfiltered nighttime longwave (LWNT) radiances increase by 0.2% for clear ocean, all-sky ocean, and land, and by 0.3% for both clear ocean and all-sky snow/ice. While a larger unfiltered longwave radiance by the CERES method is consistent with that reported by Loeb et al. (2001), the relative differences for daytime longwave are larger than that reported by Loeb et al. (2001), who reported average differences of 0.5% and 0.2% for daytime and nighttime, respectively. The average unfiltered shortwave radiance (Table 5) increases for clear ocean, clear land, and all-sky ocean by 1.1%, 1.2%, and 1.0%, respectively, while it decreases for all-sky land and all-sky snow/ice backgrounds by 0.6% and 0.4%, respectively. Loeb et al. (2001) reported a 1.6% increase for the shortwave radiance by the CERES unfiltering algorithm. A possible reason for the discrepancy may be that footprints used by Loeb et al. (2001) are predominately from the tropics, while footprints from polar regions are included in this study. In addition, Loeb et al. (2001) used the 12 standard ERBE scene types in both ERBE and CERES algorithms, while imager-derived scene information and cloud properties are used here.

5. Comparison of *NOAA-9* ERBE scanner unfiltered radiance with nonscanner measurements

The results described in section 4 show that unfiltered radiances derived using the CERES unfiltering algorithm differ from those derived by the ERBE algorithm, and those differences depend on scene type. Further, comparisons of ERBE scanner unfiltered radiances with nonscanner measurements presented in earlier studies are not applicable to radiances obtained by the CERES algorithm. Thus, to evaluate the *NOAA-9* ERBE scanner unfiltered radiances derived from the CERES unfiltering algorithm, we compare them to *NOAA-9* nonscanner observations.

The footprint size of the *NOAA-9* ERBE scanner is approximately 50 km, while the footprint size of the

TABLE 3. *NOAA-9* ERBE scanner unfiltered radiance derived by ERBE unfiltering algorithm (labeled S8) and CERES unfiltering algorithm (labeled SSF) averaged over 4 months (April, July, October, and December 1986) for LWDT. All sky (60°–90°) includes the Northern and Southern Hemispheres.

Unfiltered radiance		Clear ocean	Clear land	All-sky ocean	All-sky land	All sky (60°–90°)
Unfiltered radiance	ERBE–S8	63.40	58.85	76.21	84.46	62.27
	ERBE–SSF	64.33	59.68	77.50	86.11	63.21
	(SSF − S8) %	1.5	1.4	1.7	2.0	1.5

TABLE 4. *NOAA-9* ERBE scanner unfiltered radiance derived by ERBE unfiltering algorithm (labeled S8) and CERES unfiltering algorithm (labeled SSF) averaged over 4 months (April, July, October, and December 1986) for LWNT. All sky (60°–90°) includes the Northern and Southern Hemispheres.

Unfiltered radiance		Clear ocean	Clear land	All-sky ocean	All-sky land	All sky (60°–90°)
Unfiltered radiance	ERBE–S8	63.96	60.72	76.36	78.54	54.60
	ERBE–SSF	64.14	60.86	76.54	78.69	54.77
	(SSF − S8) %	0.3	0.2	0.2	0.2	0.3

NOAA-9 nonscanner is about 2600 km (Green and Smith 1991). For the comparison, therefore, first we need to identify *NOAA-9* ERBE scanner footprints that fall within a *NOAA-9* nonscanner footprint; second, estimate the radiance from each footprint observed from the nonscanner position, and third, integrate the estimated ERBE scanner radiances over the nonscanner FOV (Green et al. 1990). The second step requires changing the viewing geometry observed from the ERBE scanner position to the nonscanner position. The time for the ERBE scanner to cover the entire nonscanner footprint is approximately 16 min. Therefore, we need to account for the solar zenith angle change that occurs within that 16-min period for the shortwave irradiance comparison (Green et al. 1990). This section describes the process for calibrating the *NOAA-9* ERBE scanner against its nonscanner.

a. *Collocation of ERBE scanner and nonscanner footprints*

To obtain independent samples, we use only consecutive nonscanner footprints that are separated by at least 16 min. We identify all ERBE scanner footprints observed within ±8 min of the nonscanner observation time and fall within the nonscanner FOV.

b. *Simulation of nonscanner irradiance with ERBE scanner radiance measurements*

The method to estimate nonscanner irradiances by integrating ERBE scanner radiances over the nonscanner FOV was developed by Green et al. (1990) and has been applied to the ERBS nonscanner data by Bess et al. (1999) and by Rutan et al. (2001). The nonscanner measurement m at colatitude Θ and longitude Φ is the integral of the radiances, weighted by the angular response function $g(\alpha)$ of the sensor, over its FOV:

$$m(\Theta,\Phi) = \int_0^{2\pi}\int_0^{\alpha_c} L(\alpha,\beta)g(\alpha)\sin(\alpha)\,d\alpha\,d\beta, \quad (8)$$

where L is the radiance, β is the azimuth angle relative to north, α is the nadir angle, and α_c is the nadir angle limit or cutoff (62.01° for *NOAA-9*) that define the FOV of the nonscanner.

The angular response function of the sensor g is modeled as $\cos\alpha$ (Green et al. 1990). The collocated ERBE scanner radiances are used to estimate the corresponding value of m by

$$m_s(\Theta,\Phi) = \int_0^{2\pi}\int_0^{\alpha_c} L_s(\alpha_s,\beta_s)f(\alpha,\beta\,|\,\alpha_s,\beta_s)g(\alpha)\sin(\alpha)\,d\alpha\,d\beta, \quad (9)$$

where $L(\alpha_s, \beta_s)$ is the radiance observed by the ERBE scanner and subscript s indicates the ERBE scanner observation. The ERBE scanner measures the radiance at its footprint resolution on both sides of the spacecraft ground track. However, the radiance $L(\alpha,\beta)$ in Eq. (8) is observed from the nonscanner location. Even though the ERBE scanner and nonscanner are on the same spacecraft, the viewing geometries of a given ERBE scanner footprint viewed from the ERBE scanner and nonscanner positions are typically not the same. In Eq. (9) the conversion function $f(\alpha_s, \beta_s\,|\,\alpha, \beta)$ accounts for the change in the radiance observed from the ERBE scanner's viewing geometry to the nonscanner viewing geometry for all collocated ERBE scanner/nonscaner footprints. To estimate $f(\alpha_s, \beta_s\,|\,\alpha, \beta)$, we use the CERES Aqua angular distribution models (ADMs; Loeb et al. 2003) that have a collection of mean radiances as a function

TABLE 5. *NOAA-9* ERBE scanner unfiltered radiance derived by ERBE unfiltering algorithm (labeled S8) and CERES unfiltering algorithm (labeled SSF) averaged over 4 months (April, July, October, and December 1986) for SWDT. All sky (60°–90°) includes the Northern and Southern Hemispheres.

Unfiltered radiance		Clear ocean	Clear land	All-sky ocean	All-sky land	All sky (60°–90°)
Unfiltered radiance	ERBE–S8	91.53	132.54	60.07	82.28	64.36
	ERBE–SSF	92.57	134.14	59.61	81.44	64.09
	(SSF − S8) %	1.1	1.2	−0.8	−1.0	−0.4

of viewing zenith (shortwave and longwave), relative azimuth (shortwave), and solar zenith (shortwave) angles for a given scene type. Footprint location and AVHRR-derived cloud properties are used to choose ADMs for a given ERBE scanner footprint. Therefore, using the ADMs, the conversion function f is

$$f(\alpha,\beta\,|\,\alpha_s,\beta_s)=\frac{\overline{L}(\alpha,\beta)}{\overline{L}(\alpha_s,\beta_s)}=\frac{r(\alpha,\beta)}{r(\alpha_s,\beta_s)}, \qquad (10)$$

where the overbar indicates the mean radiance for a given scene type extracted from the CERES ADMs and r is the anisotropic factor.

In addition to the direction change, the solar zenith angle changes during the time when the ERBE scanner observes within the nonscanner FOV. We therefore include the effect of solar zenith angle change to the conversion function for shortwave as

$$f(\alpha,\beta\,|\,\alpha_s,\beta_s)=\frac{\overline{L}(\alpha,\beta)\cos\varsigma}{\overline{L}(\alpha_s,\beta_s)\cos\varsigma_s}=\frac{r(\alpha,\beta)\cos\varsigma}{r(\alpha_s,\beta_s)\cos\varsigma_s}, \qquad (11)$$

where ζ is the solar zenith angle at the nonscanner observation time and ζ_s is the solar zenith angle at the ERBE scanner observation time for each footprint.

To integrate Eq. (9), we discretize it using 10 zenith and 10 azimuth angular bins, the same number of bins used by Green et al. (1990). The resulting bin size is 6.2° × 36°. The discretized version of the integral form of Eq. (9) is

$$\hat{m}=\sum_{i=1}^{i=10}\sum_{j=1}^{j=10}\hat{L}_{s,ij}\cos\alpha_i\Delta\Omega_{ij}, \qquad (12)$$

where $\hat{L}_{s,ij}$ is the average of all fL_s in the ijth angular bin, and $\Delta\Omega_{ij}$ is the solid angle subtended by the ijth angular bin viewed from the nonscanner. To avoid large differences caused by undetected portions of the nonscanner FOV by the ERBE scanner, we require the scanner to fill at least 90% of the total angular bins (i.e., 90 bins). A sensitivity study by Green et al. (1990) shows that the total number of bins (i.e., angular bin size) affects the integrated ERBE scanner radiance $\hat{m}$ by less than 0.5%.

c. *Comparison of integrated radiance from* NOAA-9 *ERBE scanner with* NOAA-9 *nonscanner observations*

Following the approach discussed above, we compute the integrated ERBE scanner radiance over the collocated nonscanner FOV for *NOAA-9*. Both m and $\hat{m}$ are converted from irradiance at the nonscanner observation altitude to 30 km. The conversion factor, historically known as shape factor, depends on the angular distribution of the radiance. We apply the same shape factor for both m and $\hat{m}$, so that the relative difference is independent of the shape factor. In the remaining part of this paper, we refer to the irradiance at 30 km as the irradiance at TOA. Figure 4 shows a comparison of observed *NOAA-9* TOA nonscanner irradiance m on the x axis and the *NOAA-9* TOA-integrated ERBE scanner radiance $\hat{m}$ on the y axis for the longwave channel at night for April, July, October, and December 1986. The least squares fit lines have slopes of 0.98, 0.99, 1.00, and 1.01 for April, July, October, and December 1986, respectively, while the corresponding intercepts are 1.09, 1.20, 0.12, and −5.04 W m^{-2}, respectively. Table 6 summarizes the irradiance derived from the ERBE scanner (SC) and nonscanner (NS) and their differences. The nocturnal 4-month average longwave irradiances for the nonscanner and ERBE scanner are 229.4 and 227.8 W m^{-2}, respectively, and the difference is 1.7 W m^{-2}, indicating that the mean integrated ERBE scanner radiance is 0.7% less than the average nonscanner irradiance.

Similar to Fig. 4, Fig. 5 shows a comparison between nonscanner irradiances and integrated ERBE scanner radiances for shortwave. The least squares fit line slopes are 1.03, 1.02, 1.03, and 1.02 for April, July, October, and December, respectively, while the corresponding intercepts are −7.81, −3.54, −4.09, and 0.51 W m^{-2}, respectively. Table 6 suggests that the integrated ERBE scanner radiances are consistently higher than nonscanner irradiances for all 4 months. Averaged over 4 months, the integrated ERBE shortwave scanner radiance is 0.9% greater than the nonscanner irradiance.

As mentioned earlier, the unfiltered daytime longwave radiance is derived using filtered radiances from both the total and shortwave channels. To remove the shortwave irradiance affecting the longwave irradiance difference, we apply the coefficients derived for the shortwave comparison shown in Fig. 5. We then compare the total irradiance (shortwave + daytime longwave), so that the difference is only due to the longwave irradiance. Figure 6 shows the comparison of daytime total irradiance derived from the ERBE scanner and nonscanner. The average difference over the 4 months is 1.6 W m^{-2}, which corresponds to −0.3% of the total irradiance or −0.7% of the longwave (total minus shortwave) nonscanner irradiance.

Figure 7 shows the dependency of ERBE scanner and nonscanner irradiance differences as a function of the integrated ERBE scanner radiances. The difference is almost constant, suggesting no strong dependence of the difference on the integrated ERBE scanner radiance. In addition, we use the Student's t test for paired data at the 5% significance level to check if two sample means are

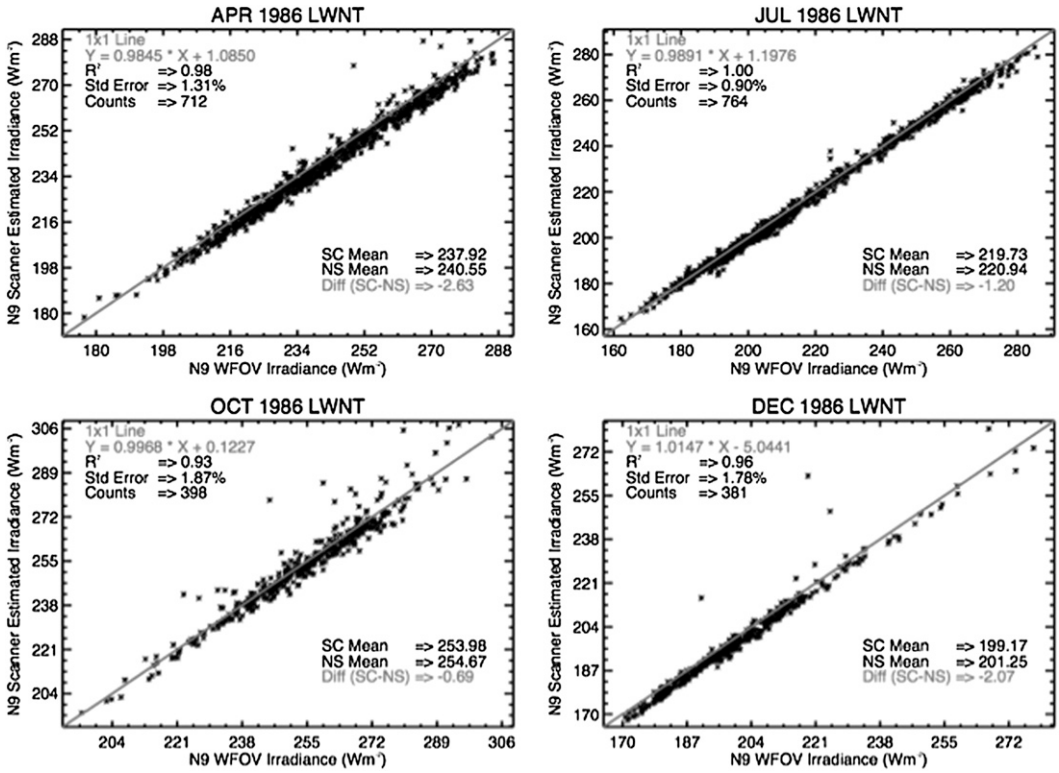

FIG. 4. Scatterplots of *NOAA-9* WFOV nonscanner irradiance ($\mathrm{W\,m^{-2}}$) at the TOA vs integrated *NOAA-9* ERBE scanner radiances ($\mathrm{W\,m^{-2}}$) over the FOV of the nonscanner for LWNT. Each data point represents one collocated sample in a month. The gray line is the one-to-one line with the slope and intercept indicated with gray letters in the plots.

different. To perform this test, we divide the mean difference by the standard deviation of the differences between the matched footprints over 4 months of data. The numbers of matched samples are 2255, 1842, and 1825 for nighttime longwave and shortwave, and daytime total irradiances, respectively. The standard deviations of the matched differences are 3.34, 5.21, and 5.18 $\mathrm{W\,m^{-2}}$ for nighttime longwave and shortwave, and total irradiances, respectively. The test resulted in the absolute z values of 24.3, 16.9, and 12.6 for the nighttime longwave and shortwave, and daytime total channels, respectively. Because the z values are quite large for all three channels at the 5% significance level, this test rejects the null hypothesis of equality of means with 95% confidence, indicating the differences between the nonscanner irradiances and integrated ERBE scanner radiances are statistically significant.

In addition to instrument uncertainty, there is uncertainty associated with the ADMs used in the process of changing the observation position of the ERBE scanner to the nonscanner. We quantify the uncertainty due to the use of ADMs in the next section.

d. Uncertainty in the comparison result

The CERES ADMs are built based on the scene identification used in the edition 2 (Ed2) CERES cloud algorithm (Minnis et al. 2008, 2011). Even though the anisotropic factors in ADMs contain error, the error in the irradiance is relatively small when mean irradiance is computed using irradiances over a wide range of viewing geometries because angle-dependent errors partially cancel each other. However, when the direction of radiance is changed from the ERBE scanner to the nonscanner viewing geometry, the viewing angle is systematically changed from a smaller viewing angle of the ERBE scanner to a larger viewing angle toward the nonscanner (Fig. 8). Therefore, estimating the irradiance over the nonscanner FOV from ERBE scanner radiances using ADMs is more vulnerable to the ADM error. To examine the effect of the ADM error to the comparisons discussed in the previous section, we assume that the anisotropic factor in the CERES ADMs contains a 5% error. When applying Eq. (9), we increase the ADM radiance by 5% when the anisotropic factor is greater than 1 (i.e., oblique view for shortwave and nadir view

TABLE 6. *NOAA-9* nonscanner irradiance and integrated ERBE scanner radiance comparison for different months.

	Longwave nighttime			Shortwave daytime			Total daytime (SWDT + LWDT)*		
Month	NS mean	SC mean	% diff	NS mean	SC mean	% diff	NS mean	SC mean	% diff
Apr 1986	240.6	237.9	−1.1	229.2	229.3	0.0	472.0	469.7	−0.5
Jul 1986	220.9	219.7	−0.5	281.5	282.5	0.3	522.2	521.2	−0.2
Oct 1986	254.7	254.0	−0.3	201.2	204.0	1.4	463.8	464.8	0.2
Dec 1986	201.2	199.2	−1.0	268.9	274.4	2.0	505.8	501.4	−0.9
Mean	229.4	227.7	−0.7	245.2	247.5	0.9	490.9	489.3	−0.3

* The 4-month average relative difference for LWDT irradiance is obtained by subtracting the SWDT irradiance from total irradiance during the day $[(489.3 - 245.2) - (490.9 - 245.2)]/(490.9 - 245.2) = -0.0065$, i.e., −0.7%.

for longwave) and decrease it by 5% when the anisotropic factor is smaller than 1 (i.e., near-nadir view for shortwave and oblique view for longwave), causing the scenes to be more anisotropic. Because ADMs are used to change the direction from a smaller viewing zenith to a larger viewing zenith, we expect that the integrated radiance from the ERBE scanner would decrease (increase) for shortwave (longwave). Table 7 shows the mean differences between the nonscanner irradiance and integrated ERBE scanner radiance after perturbing the ADM radiance. When the anisotropic factor is changed by 5%, the 4-month mean differences between the nonscanner irradiance and integrated ERBE scanner radiance are 6.7% and −2.5% for shortwave and longwave, respectively. This translates to a 5.8% increase for shortwave and 1.8% decrease for longwave from the unperturbed results.

We interpret this sensitivity result in the context of the uncertainty of the scanner–nonscanner irradiance comparison in the following way. Loeb et al. (2007) show that the irradiance derived from near-nadir view (viewing zenith angle less than 5°) and oblique view (viewing zenith angle between 50° and 60°) differ, on average, by 5.3% for shortwave and by less than 3% for longwave. Because the relative difference of the ADM-derived irradiance is equivalent to the relative error in the anisotropic factor, the relative errors in the anisotropic factor at the nadir and oblique views can be ~5% for

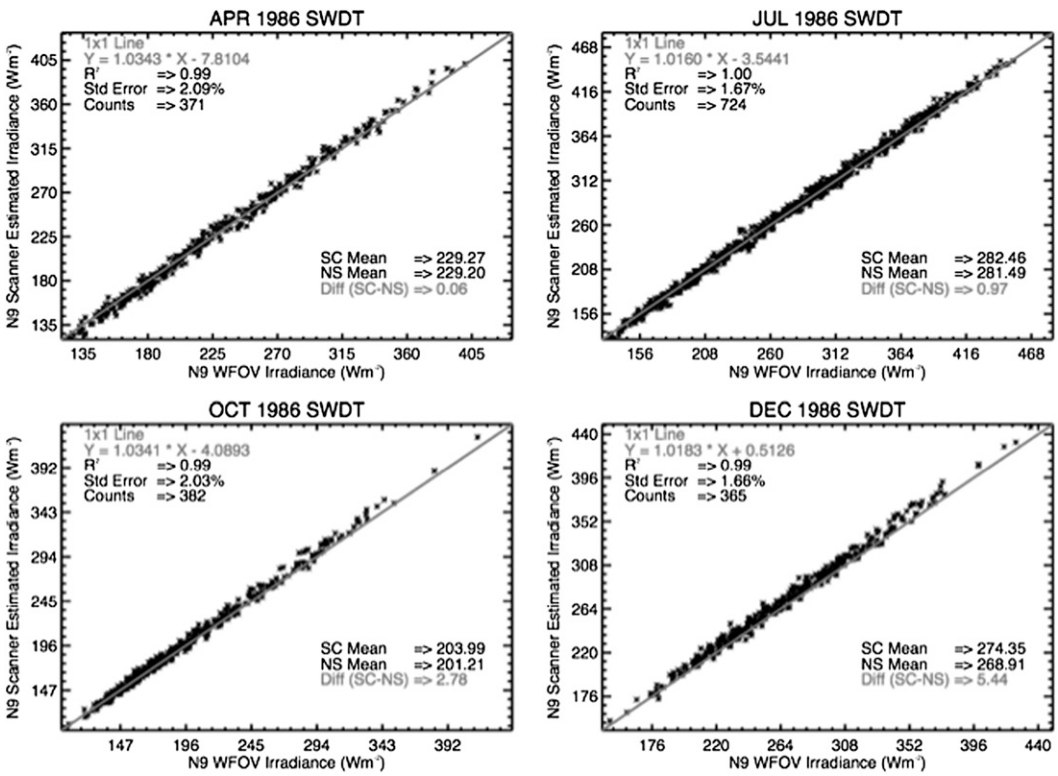

FIG. 5. As in Fig. 4, but for SWDT.

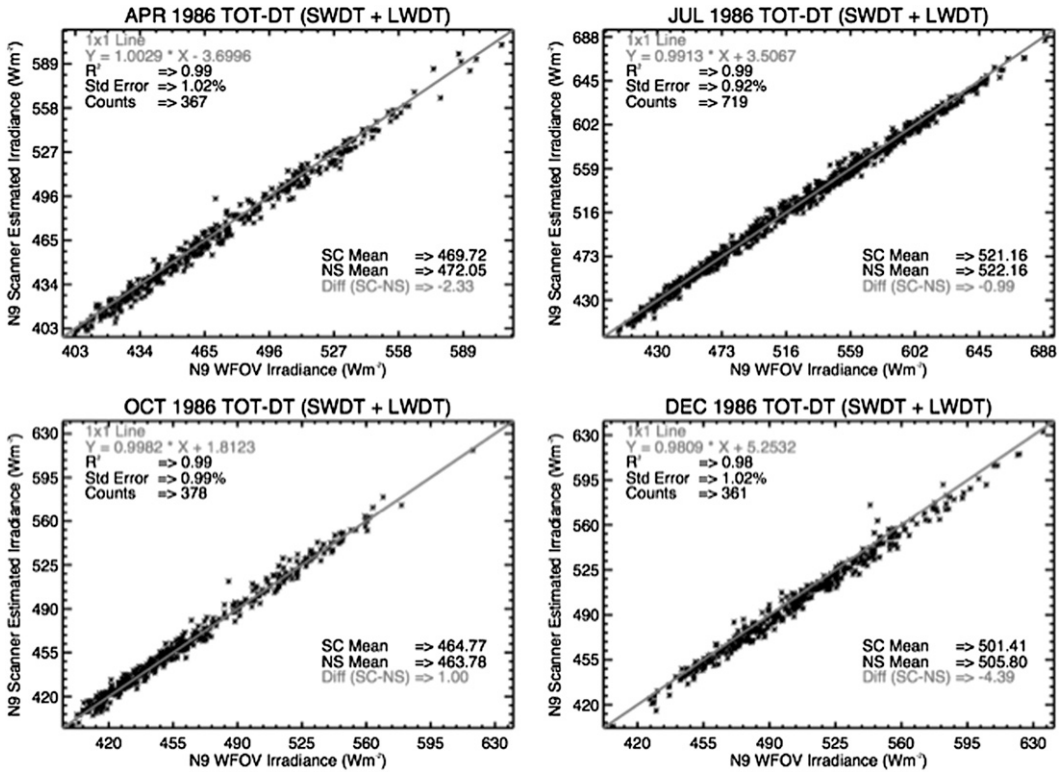

FIG. 6. As in Fig. 4, but for the total.

shortwave and ~3% for longwave. A 5% perturbation of the anisotropic factor in the opposite direction at nadir and oblique views used in the sensitivity study corresponds to a 10% anisotropic factor difference between the nadir and oblique views. Therefore, the uncertainty envelope due to the ADM error is 2.9% (half of 5.8%) for shortwave and 0.6% (one-third of 1.8%) for longwave. Because the sign of the bias error in the anisotropic factor is unknown, we split the envelope equally so that half is on the positive side and the other half is on the negative side. This argument leads to the range of the relative difference between nonscanner irradiance and integrated ERBE scanner radiance being 0.9% ± 1.5% for shortwave and −0.7% ± 0.3% for nighttime longwave. We assume that the uncertainty in the daytime longwave is $(1.5^2 + 0.3^2)^{1/2} = 1.5\%$ because the daytime longwave measurements are derived from total and shortwave measurements. The range of relative difference for daytime longwave is therefore −0.7% ± 1.5%.

Another possible source of error is the uncertainty associated with scene identification. The ADM is determined based on the scene type of the ERBE scanner footprint derived from AVHRR. To assess the uncertainty due to cloud properties, we perturb the cloud fraction by ±0.05 (5%) and the logarithmic mean cloud optical thickness by 0.1 (approximately 10% increase of the optical thickness). The result averaged over 4 seasonal months is shown in Table 8. Increasing (decreasing) the cloud fraction by 0.05 decreases (increases) the integrated ERBE scanner radiance by 0.1% (0.01%) for nighttime longwave and 0.2% (0.01%) for daytime longwave. Similarly, increasing and decreasing the cloud fraction by 0.05 increases the integrated ERBE scanner radiance by 0.5% and 0.1% for shortwave. The integrated ERBE scanner radiance changes by a similar magnitude when optical thickness is perturbed by 10%. A 0.05 cloud fraction and 10% optical thickness are realistic uncertainties in these retrieved variables (Kato et al. 2011). The result shows that the irradiance change is one order of magnitude smaller than the change caused by the anisotropic factor. In addition, cloud fraction and optical thickness error affect the selection of ADMs, hence the anisotropic factor. We therefore conclude that the uncertainty in the integrated ERBE scanner radiance is dominated by the uncertainty in the anisotropic factor. Estimated uncertainties are ±0.3% for nighttime longwave and ±1.5% for shortwave and daytime longwave.

The calibration uncertainty ($k = 1$ or 1σ) of the ERBE scanner is 1% for total and longwave channels and 2% for the shortwave channel (Wielicki et al. 1995). We take the ERBS and *NOAA-9* nonscanner differences discussed

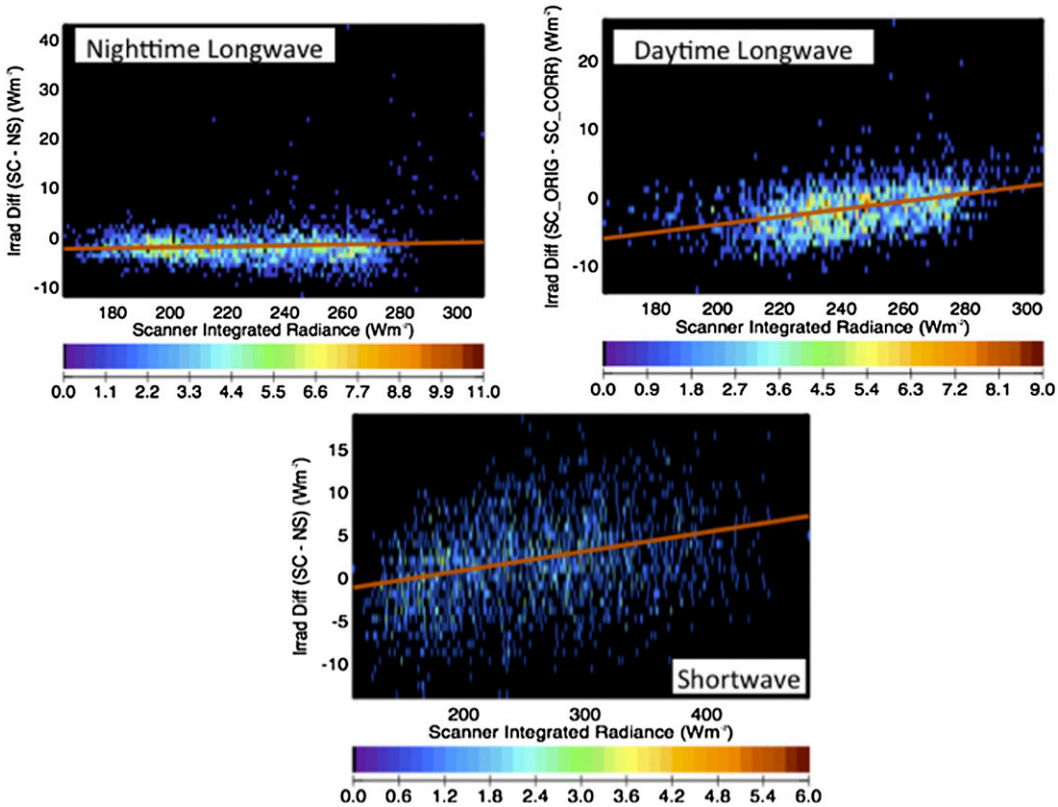

FIG. 7. A 2D histogram of matched footprints between *NOAA-9* ERBE scanner and nonscanner with ERBE scanner integrated radiance on the abscissa and the difference of ERBE scanner integrated radiance and nonscanner irradiance on the ordinate. All 4 months of data are combined for these plots.

in section 6 as the uncertainties in the *NOAA-9* nonscanner irradiances. If we add uncertainties due to instrument calibrations and the anisotropic factor, then the nonscanner and ERBE scanner irradiances agree to within $(1^2 + 0.6^2 + 0.3^2)^{1/2} = 1.2\%$ for nighttime longwave, $(1^2 + 0.4^2 + 1.5^2)^{1/2} = 1.8\%$ for daytime longwave, and $(2^2 + 0.3^2 + 1.5^2)^{1/2} = 2.5\%$ for shortwave. We need to make several assumptions to conclude that the *NOAA-9* ERBE scanner unfiltered radiance is biased by 0.9% for shortwave and −0.7% for both daytime and nighttime longwave: 1) footprint matching uncertainty that causes the difference between nonscanner irradiance and integrated ERBE scanner radiance is negligible and 2) the uncertainty of the difference is dominated by instrument calibrations. Though we have not quantified the effect of the first assumption, the sign of the difference is consistent for 4 months, implying that the difference is bias and increasing the number of matched samples may not reduce the difference. In fact, the relative difference averaged over 12 months in 1986 is 1.0%, −0.2%, and −0.1% for shortwave, nighttime longwave, and daytime longwave, respectively. The relative differences have the same sign as the corresponding 4-month average, and the difference between the 4- and 12-month averages are within the instrument uncertainty. For the second assumption, although other components are not negligible, we showed in this section that the calibration uncertainty is the largest component for nighttime longwave and shortwave. Therefore, calibration is more likely to cause the difference than the uncertainty due to ADMs.

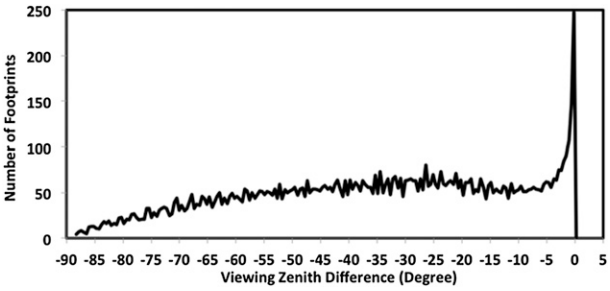

FIG. 8. Probability distribution function of viewing zenith angle difference defined as viewing zenith angle viewed from the ERBE scanner position minus the viewing zenith viewed from the nonscanner position for the same ERBE scanner footprint.

TABLE 7. Anisotropic factor sensitivity to LW and SW irradiance comparisons using CERES ADMs.

Month	LW nighttime (NS − SC)	LW nighttime % diff	LWDT (NS − SC)	LWDT % diff	SWDT (NS − SC)	SWDT % diff
Apr 1986	−6.9	−2.9	−6.8	−2.8	12.7	5.5
Jul 1986	−5.2	−2.4	−5.4	−2.3	14.2	5.0
Oct 1986	−5.1	−2.0	−3.6	−1.4	17.3	8.6
Dec 1986	−5.7	−2.8	−8.6	−3.6	20.1	7.5
Mean	−5.7	−2.5	−6.1	−2.5	16.1	6.7

If we treat these uncertainties as the envelope of a bias error with unknown sign in the *NOAA-9* ERBE scanner unfiltered radiances, and assume that the stability of the nonscanner is much better, then we could adjust ERBE scanner-derived irradiances by the relative difference averaged over the 4 or 12 months to be consistent with the ERBS and *NOAA-9* nonscanners to within their uncertainties; that is, the adjustment calibrates the *NOAA-9* shortwave and longwave unfiltered radiances against the *NOAA-9* nonscanner. Note that the result of this study does not depend significantly on cloud properties derived from AVHRR used for scene identification of ERBE scanner footprints. This is because cloud optical thicknesses derived from AVHRR are adjusted so that the relationship of the ERBE radiance as a function of the logarithm of the product of cloud fraction f and cloud optical thickness $\tau \log(f\tau)$ for a given viewing geometry is forced to be the same as the relationship between CERES radiance and $\log(f\tau)$ derived from MODIS. In other words, AVHRR-derived cloud properties are corrected to agree with cloud properties derived from MODIS. For the absolute calibration of the nonscanners, constraining the global and annual mean TOA net irradiance by a long-term mean ocean heating is necessary, as demonstrated by Loeb et al. (2009), for CERES-derived global annual mean TOA shortwave and longwave irradiances.

6. Comparison of *NOAA-9* and ERBS nonscanner measurements

The ERBS nonscanner measurements overlap with CERES TRMM measurements, providing a long-term record that has been analyzed by Wielicki et al. (2002) and Wong et al. (2006). In addition, Smith et al. (2006) compared the radiation budget measured from different instruments. Therefore, comparisons between the *NOAA-9* and ERBS nonscanners can be used to assess *NOAA-9* nonscanner and ERBE scanner calibrations relative to ERBS and, in turn, TRMM CERES. Rutan et al. (2001) showed that the ERBS nonscanner irradiances are consistent with the CERES TRMM scanner measurements to better than 1.5%, 2%, and 1% for shortwave and longwave at day and night, respectively. This study compares 2 years (January 1985–December 1986) of nonscanner observations from the *NOAA-9* and ERBS S7 data products. The ERBE S7 data product is a monthly product and contains instantaneous irradiances derived from nonscanner observations (Barkstrom and Wong 2013). Similar to the *NOAA-9* ERBE scanner and nonscanner comparison performed above, the nonscanner comparison also requires collocation of their footprints. To ensure the footprint collocation, matched footprints are observed within 8 min apart, and the angle between the lines connecting the center of the footprints and the center of the earth computed from ERBS and *NOAA-9* nonscanner footprints (the earth central angle) is within 5°. According to Green and Smith (1991), the irradiance derived from nonscanners is equivalent to ERBE scanner-derived irradiances averaged over 7° and 11° of the earth central angle for the ERBS and *NOAA-9* nonscanners, respectively. These correspond to approximately 1600- and 2400-km footprint sizes. Restricting the earth central angle between the center of collocated *NOAA-9* and ERBS footprints to less than 5° ensures that the ERBS nonscanner footprint falls

TABLE 8. Cloud property sensitivity to LW and SW irradiance comparisons using CERES ADMs.

4 months' avg diff	LWNT (SC − NS)	LWNT (NS − SC)/(SC) %	LWDT (SC − NS)	LWDT (NS − SC)/(SC) %	SWDT (SC − NS)	SWDT (NS − SC)/(SC) %
0.05 increase in cloud fraction	−1.7	−0.8	−2.1	−0.9	3.3	1.4
0.05 decrease in cloud fraction	−1.6	−0.7	−1.7	−0.7	2.5	1.0
0.1 increase in cloud fraction	−1.6	−0.7	−1.6	−0.7	1.8	0.7
0.1 decrease in cloud fraction	−1.7	−0.8	−1.7	−0.7	2.8	1.2

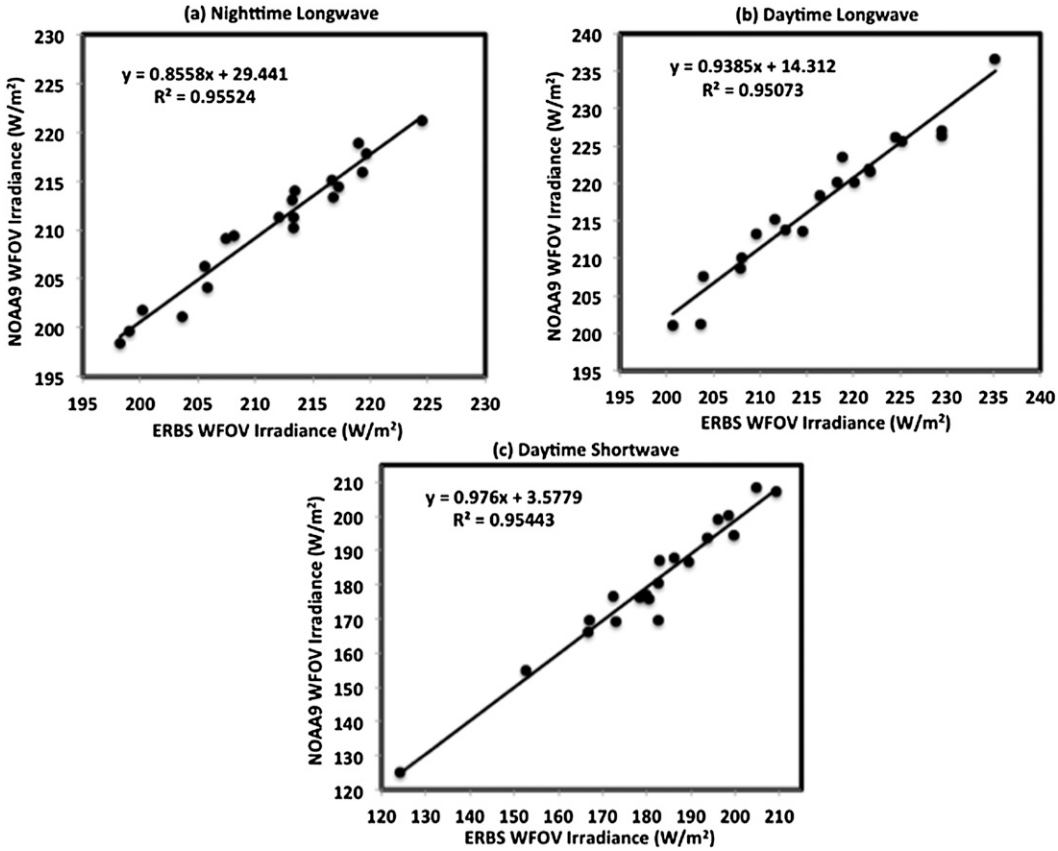

FIG. 9. Matched ERBS (abscissa) and *NOAA-9* (ordinate) nonscanner-derived irradiances for (a) LWNT, (b) LWDT, and (c) SWDT. Instantaneous irradiances are averaged over a month and each point represents monthly-mean irradiance. Two years of data, from January 1985 through December 1986, are used. Irradiances are computed at the satellite altitude. The line is the linear regression line, and the slope and intercept are shown in the plot; R^2 is the correlation coefficient.

completely within its *NOAA-9* counterpart. When the ERBS nonscanner footprint is completely within the *NOAA-9* nonscanner FOV, the ERBS nonscanner footprint covers only 44% of the area covered by the *NOAA-9* FOV. As a result, the comparison of instantaneous irradiances is noisy. Therefore, instantaneously matched irradiances are averaged over a month and monthly-mean values from *NOAA-9* and ERBS nonscanners are used for the comparison.

ERBS and NOAA-9 *nonscanner irradiance*

Monthly-mean daytime and nighttime longwave and shortwave irradiances for both the ERBS and *NOAA-9* nonscanner are computed separately after collocating footprints. Figures 9a–c show the monthly-mean nighttime longwave, and daytime longwave and daytime shortwave irradiances, respectively. The ERBS nonscanner irradiance is on the x axis, and the *NOAA-9* nonscanner irradiance is on the y axis. The relatively large scatter arises for several reasons. First, as mentioned earlier, the ERBS FOV covers only 44% of the *NOAA-9* nonscanner FOV. Second, the effect of the shape factor discussed in Green and Smith (1991) is not accounted for in this comparison because we used irradiances measured at satellite altitudes and simply scaled the *NOAA-9* irradiance to the ERBS altitude by the ratio of the inverse square of the distance from the center of the earth.

To estimate the impact of these issues, we use multiple (at least two) ERBS nonscanner footprints within a *NOAA-9* nonscanner footprint to estimate the variability of the scene. We then use a 5% standard deviation of ERBS nonscanner irradiance relative to their mean as a threshold to select footprints with a relatively uniform scene. This screening reduces the total number of footprints to 36% for shortwave, 76% for nighttime longwave, and 69% for daytime longwave relative to those without screening. Table 9 shows that the absolute value of relative differences changes minimally with the screening, while the sign of the relative difference

TABLE 9. Comparison of 2 years (from January 1985 through December 1986) matched ERBS and *NOAA-9* nonscanner irradiances averaged over a month. Screening means that the standard deviation of ERBS irradiance within a *NOAA-9* footprint is used to select uniform scenes.

	Avg irradiance over 2 yr without screening (with screening)		*NOAA-9* − ERBS without screening (with screening)		(*NOAA-9* − ERBS)/ERBS without screening (with screening)	
	ERBS (W m^{-2})	*NOAA-9* (W m^{-2})	Diff (W m^{-2})	RMS (W m^{-2})	Relative diff (%)	Relative RMS (%)
LWNT	211.3 (215.3)	210.3 (214.0)	−1.0 (−1.4)	1.4 (1.6)	−0.5 (−0.6)	0.6 (0.7)
SWDT	181.1 (158.0)	180.3 (158.3)	−0.8 (0.4)	4.0 (4.7)	−0.4 (0.3)	2.2 (3.0)
LWDT	216.6 (220.0)	217.6 (220.8)	1.0 (1.0)	2.0 (2.0)	0.5 (0.4)	0.9 (0.9)

changes for shortwave. This is probably caused by scenes that affect the shape factor needed to convert nonscanner irradiance from satellite altitude to a different altitude. A simple scaling by the square of the distance assumes the scene is Lambertian and introduces a bias error of about −2% when converting irradiance at an altitude of 580 km to that at 30 km (Green and Smith 1991). If the error changes linearly with the distance, then the *NOAA-9* irradiance at the satellite altitude of 812 km needs to be increased by 0.7% when converting it to the ERBS satellite altitude at 610 km. Therefore, a 0.7% increase in the shortwave irradiance might be caused by selecting more uniform scenes. For this reason, we conclude that the relative differences between ERBS and *NOAA-9* nonscanners are 0.3% for shortwave, −0.6% for nighttime longwave, and 0.4% for daytime longwave.

7. Summary and conclusions

Four months (April, July, October, and December 1986) of the *NOAA-9* ERBE scanner S8 data product were used to generate an ERBE IES similar to a CERES IES. The CERES unfiltering algorithm was then applied to the ERBE IES to derive a new set of unfiltered radiances. The unfiltering process eliminates the effect of the instrument response function and separates the earth reflected solar radiance from the earth emitted thermal radiance. Cloud properties derived from AVHRR observations were collocated within the ERBE scanner footprints and used to identify the scene type required for the CERES unfiltering algorithm. The CERES algorithm increases the unfiltered longwave radiances by 1.4% to 2.0% and by 0.2% to 0.3% for daytime and nighttime, respectively. Similarly, the unfiltered shortwave radiance increases by ~1% for clear ocean and land, while it decreases for all-sky ocean, land, and snow/ice by 0.8%, 1.0%, and 0.4%, respectively.

We compared the ERBE scanner and nonscanner on board *NOAA-9* by collocating their footprints and integrating ERBE scanner radiances over the nonscanner FOV. In the comparison process, the radiance observed from the ERBE scanner position is turned to that observed from the nonscanner position using CERES *Aqua* Ed2 ADMs. The scene type is determined using the AVHRR cloud property dataset. The integrated ERBE scanner radiance is larger by 0.9% compared to the nonscanner irradiance for shortwave, while it is lower by 0.7% for both daytime and nighttime longwave. In addition, we investigated the uncertainty caused by the uncertainty in the anisotropic factor in the *Aqua* ADMs caused by the error in the cloud fraction and cloud optical thickness through sensitivity studies. Based on the sensitivity study, we conclude that the 1σ uncertainty range by this process is ±1.5%, ±0.3% and ±1.5% for shortwave, and nighttime and daytime longwave, respectively.

In addition, we compared the *NOAA-9* nonscanner irradiances with the ERBS nonscanner irradiances using 2 years of data, from January 1985 through December 1986. The mean relative difference in the irradiance was computed by using collocated footprints with relatively uniform scenes. The uniform scenes were selected based on the standard deviation of irradiance obtained from the ERBS nonscanner footprints, which are within a *NOAA-9* nonscanner footprint. The *NOAA-9* nonscanner irradiances are larger by 0.3%, smaller by 0.6%, and larger by 0.4% relative to the ERBE nonscanner, for shortwave, and nighttime and daytime longwave, respectively.

Taking into account the instrument calibration uncertainty for both the ERBE scanner and nonscanner, the *NOAA-9* ERBE scanner unfiltered radiance uncertainties are ±2.5%, ±1.2%, and ±1.8% in the shortwave, nighttime longwave, and daytime longwave, respectively. If we assume a negligible uncertainty due to collocating the *NOAA-9* and ERBS nonscanner footprints and that the ERBE scanner calibration error predominately causes the ERBE scanner and nonscanner irradiance difference, then the *NOAA-9* ERBE scanner radiances in the shortwave, nighttime longwave, and daytime longwave are biased by 0.9%, −0.7%, and −0.7% respectively, relative to *NOAA-9* nonscanner observations.

The unfiltering of *NOAA-9* ERBE scanner radiance using the CERES algorithm discussed in this study is a first step in the reprocessing of ERBE data using CERES algorithms to eliminate the algorithm inconsistency between the ERBE and CERES data. In addition, comparisons of *NOAA-9* ERBE scanner and nonscanner observations and *NOAA-9* and ERBS nonscanner observations performed in this study can be used to bring the *NOAA-9* ERBE scanner unfiltered radiances to the same radiometric scale of the *NOAA-9* nonscanner and, in turn, with the ERBS nonscanner, which has an overlap with the TRMM CERES instrument. Further, improving the unfiltering process of ERBE nonscanners based on what we learned from the CERES project is currently taking place. By making these various measurements more consistent, it will be possible to better characterize the variations in the radiation budget over long time scales and how they impact the climate.

Acknowledgments. We thank Drs. Bruce Wielicki, Norman G. Loeb, and David Johnson, and Mr. David Doelling for useful discussions. This work was supported by the NOAA Climate Data Record program (http://www.ncdc.noaa.gov/cdr).

REFERENCES

Arduini, R. F., 1985: Solar radiance models for determination of ERBE scanner filter factor. Contractor Rep. 172595, 40 pp. [Available from NASA Langley Research Center, MS 420, Hampton, VA 23681.]

Barkstrom, B. R., 1984: The Earth Radiation Budget Experiment (ERBE). *Bull. Amer. Meteor. Soc.,* **65,** 1170–1185, doi:10.1175/1520-0477(1984)065<1170:TERBE>2.0.CO;2.

——, and G. L. Smith, 1986: The Earth Radiation Budget Experiment: Science and implementation. *Rev. Geophys.,* **24,** 379–390, doi:10.1029/RG024i002p00379.

——, and J. F. Kibler, cited 2013: Earth Radiation Budget Experiment. [Available online at http://badc.nerc.ac.uk/data/gedex/detail/erbe.det.]

——, and T. Wong, cited 2013: Earth Radiation Budget Experiment (ERBE) for Monthly Medium-Wide Data Tape (MWDT) (S-7). Langley ASDC Dataset Doc. [Available online at http://eosweb.larc.nasa.gov/GUIDE/dataset_documents/erbe_s7.html.]

Bess, T. D., G. L. Smith, K. A. Bush, and D. A. Rutan, 1999: Intercomparison of ScaRaB and ERBS monthly mean radiation fluxes. Preprints, *10th Conf. on Atmospheric Radiation,* Madison, WI, Amer. Meteor. Soc., 60–63.

Bloom, S. A., and Coauthors, 2005: Documentation and validation of the Goddard Earth Observing System (GEOS) Data Assimilation System—Version 4. Technical Report Series on Global Modeling and Data Assimilation, Vol. 26, NASA Tech. Memo. NASA/TM-2005-104606, 181 pp.

Green, N. R., and G. L. Smith, 1991: Shortwave shape factor inversion of earth radiation budget observations. *J. Atmos. Sci.,* **48,** 390–402, doi:10.1175/1520-0469(1991)048<0390:SSFIOE>2.0.CO;2.

——, and L. M. Avis, 1996: Validation of ERBS scanner radiances. *J. Atmos. Oceanic Technol.,* **13,** 851–862, doi:10.1175/1520-0426(1996)013<0851:VOESR>2.0.CO;2.

——, B. F. House, P. W. Stackhouse, W. Xiangqian, S. A. Ackerman, W. L. Smith, and M. J. Johnson, 1990: Intercomparison of scanner and nonscanner measurements for the Earth Radiation Budget Experiment. *J. Geophys. Res.,* **95,** 11 785–11 798, doi:10.1029/JD095iD08p11785.

Gruber, A., R. Ellingson, P. Ardanuy, M. Weiss, S. K. Yang, and S. N. Oh, 1994: A comparison of ERBE and AVHRR longwave flux estimates. *Bull. Amer. Meteor. Soc.,* **75,** 2115–2130, doi:10.1175/1520-0477(1994)075<2115:ACOEAA>2.0.CO;2.

Kato, S., S. Sun-Mack, W. F. Miller, F. G. Rose, Y. Chen, P. Minnis, and B. A. Wielicki, 2010: Relationship among cloud occurrence frequency, overlap, and effective thickness derived from CALIPSO and CloudSat merged cloud vertical profiles. *J. Geophys. Res.,* **115,** D00H28, doi:10.1029/2009JD012277.

——, and Coauthors, 2011: Improvement of top-of-atmosphere and surface irradiance computations with CALIPSO-, CloudSat-, and MODIS-derived cloud and aerosol properties. *J. Geophys. Res.,* **116,** D19209, doi:10.1029/2011JD016050.

Kopia, L. P., 1986: Earth Radiation Budget Experiment scanner instrument. *Rev. Geophys.,* **24,** 400–406, doi:10.1029/RG024i002p00400.

Kusterer, J. M., cited 2013: NASA Langley ASDC user services. [Available online at http://ceres.larc.nasa.gov/documents/DPC/DPC_current/pdfs/DPC_IES_R3V1.pdf.]

Liu, X., W. L. Smith, D. K. Zhou, and A. Larar, 2006: Principal component-based radiative transfer model for hyperspectral sensors: Theoretical concept. *J. Appl. Opt.,* **45,** 201–209, doi:10.1364/AO.45.000201.

Loeb, N. G., K. J. Priestly, D. P. Kratz, E. B. Geier, R. N. Green, and B. A. Wielicki, 2001: Determination of unfiltered radiances from the Clouds and the Earth's Radiant Energy System instrument. *J. Appl. Meteor.,* **40,** 822–825, doi:10.1175/1520-0450(2001)040<0822:DOURFT>2.0.CO;2.

——, N. Nanalo-Smith, S. Kato, W. F. Miller, S. K. Gupta, P. Minnis, and B. A. Wielicki, 2003: Angular distribution models for top-of-atmosphere radiative flux estimation from the Clouds and the Earth's Radiant Energy System instrument on the Tropical Rainfall Measuring Mission satellite. Part I: Methodology. *J. Appl. Meteor.,* **42,** 240–265, doi:10.1175/1520-0450(2003)042<0240:ADMFTO>2.0.CO;2.

——, S. Kato, K. Loukachine, N. Manalo-Smith, and D. R. Doelling, 2007: Angular distribution models for top-of-atmosphere radiative flux estimation from the Clouds and the Earth's Radiant Energy System instrument on the *Terra* Satellite. Part II: Validation. *J. Appl. Meteor. Climatol.,* **24,** 564–584, doi:http://dx.doi.org/10.1175/JTECH1983.1

——, B. A. Wielicki, D. R. Doelling, G. L. Smith, D. F. Keyes, S. Kato, N. Manalo-Smith, and T. Wong, 2009: Toward optimal closure of the earth's top-of-atmosphere radiation budget. *J. Climate,* **22,** 748–766, doi:10.1175/2008JCLI2637.1.

Luther, M. R., J. E. Cooper, and G. R. Taylor, 1986: The Earth Radiation Budget Experiment nonscanner instrument. *Rev. Geophys.,* **24,** 391–399, doi:10.1029/RG024i002p00391.

Minnis, P., and Coauthors, 2008: Cloud detection in nonpolar regions for CERES using TRMM VIRS and Terra and Aqua MODIS data. *IEEE Trans. Geosci. Remote Sens.,* **46,** 3857–3884, doi:10.1109/TGRS.2008.2001351.

——, and Coauthors, 2011: CERES edition-2 cloud property retrievals using TRMM VIRS and Terra and Aqua MODIS

data—Part I: Algorithms. *IEEE Trans. Geosci. Remote Sens.,* **49,** 4374–4400, doi:10.1109/TGRS.2011.2144601.

Rutan, D. A., G. L. Smith, R. B. Lee III, and T. Wong, 2001: Intercomparison of CERES scanning and ERBS WFOV nonscanning radiometers. Preprints, *11th Conf. on Satellite Meteorology and Oceanography,* Madison, WI, Amer. Meteor. Soc., P5.28. [Available online at https://ams.confex.com/ams/11satellite/techprogram/paper_24163.htm.]

Smith, G. L., Z. P. Szweczyk, D. A. Rutan, and R. B. Lee III, 2006: Comparison of measurements from satellite radiation budget instruments. *J. Geophys. Res.,* **111,** D04101, doi:10.1029/2005JD006307.

Suttles, J. T., B. A. Wielicki, and S. Vemury, 1992: Top-of-atmosphere radiative fluxes: Validation of ERBE scanner inversion algorithm using *Nimbus-7* ERB data. *J. Appl. Meteor.,* **31,** 784–796, doi:10.1175/1520-0450(1992)031<0784:TOARFV>2.0.CO;2.

Trepte, Q. Z., P. Minnis, and R. F. Arduini, 2003: Daytime and nighttime polar cloud and snow identification using MODIS data. *Optical Remote Sensing of the Atmosphere and Clouds III,* H.-L. Huang, D. Lu, and Y. Sasano, Eds., International Society for Optical Engineering (SPIE Proceedings, Vol. 4891), 449–459, doi:10.1117/12.467306.

USGS, cited 2013: Table 1—AVHRR spectral channels, resolution, and primary uses. [Available online at http://ivm.cr.usgs.gov/tables.php.]

Vincent, K., cited 2013: Orbital information. NOAA polar orbiter data user's guide. [Available online at http://www.ncdc.noaa.gov/oa/pod-guide/ncdc/docs/podug/html/c1/sec1-2.htm.]

Wielicki, B. A., and R. N. Green, 1989: Cloud identification for ERBE radiative flux retrieval. *J. Appl. Meteor.,* **28,** 1133–1146, doi:10.1175/1520-0450(1989)028<1133:CIFERF>2.0.CO;2.

——, R. D. Cess, M. D. King, D. A. Randall, and E. F. Harrison, 1995: Mission to planet Earth: Role of clouds and radiation in climate. *Bull. Amer. Meteor. Soc.,* **76,** 2125–2153, doi:10.1175/1520-0477(1995)076<2125:MTPERO>2.0.CO;2.

——, and Coauthors, 1998: Clouds and the Earth's Radiant Energy System (CERES): Algorithm overview. *IEEE Trans. Geosci. Remote Sens.,* **36,** 1127–1141, doi:10.1109/36.701020.

——, and Coauthors, 2002: Evidence for large decadal variability in the tropical mean radiative energy budget. *Science,* **295,** 841–843, doi:10.1126/science.1065837.

Wong, T., 2013: Earth Radiation Budget Experiment (ERBE) S-8 processed archival tape (PAT) data in native (NAT) format. Langley ASDC Dataset Doc. [Available online at http://eosweb.larc.nasa.gov/GUIDE/dataset_documents/erbe_s8.html.]

——, B. A. Wielicki, R. B. Lee III, G. L. Smith, K. A. Bush, and J. K. Willis, 2006: Reexamination of the observed decadal variability of the earth radiation budget using altitude-corrected ERBE/ERBS nonscanner WFOV data. *J. Climate,* **19,** 4028–4040, doi:10.1175/JCLI3838.1.